



# Measurement report: Significant ozone loss during winter 2020 measured from ground based microwave radiometer

Richard Johansson<sup>1</sup>, Uwe Raffalski<sup>1</sup>, Mathias Milz<sup>2</sup>, and Jochen Groß<sup>3</sup>

<sup>1</sup>Swedish Institute of Space Physics, Kiruna, Sweden

<sup>2</sup>Division of Space Technology, Department of Computer Science, Electrical and Space Engineering, Luleå University of Technology, Kiruna, Sweden

<sup>3</sup>Karlsruhe Institute of Technology, Karlsruhe, Germany

**Correspondence:** Richard Johansson (richard.johansson@irf.se)

**Abstract.** Ground-based microwave observations from MIRA2 situated in Kiruna, Sweden, were used to investigate Arctic stratospheric ozone during the winter 2019/2020. A comparison of O<sub>3</sub> retrievals with coincident measurements of Aura MLS between 1 October 2019 and 30 April 2020 shows good agreement across the investigated pressure levels (74, 56, 46, and 10 hPa). Remaining differences are well within the retrieval uncertainty of MIRA2. This demonstrates the capability of MIRA2 to provide robust ozone measurements for studies of stratospheric variability.

A tracer-based approach was applied to derive cumulative chemical ozone loss on isentropic surfaces. At the 475 K level, ozone depletion increased from late winter into early spring, reaching a maximum loss of  $2.19 \pm 0.90$  ppmv in early April 2020. The magnitude and timing of the loss are consistent with the exceptional Arctic ozone depletion stated by model simulations and satellite-based estimates during the winter 2019/2020 and agree well. Despite limited temporal sampling, the tracer-based method enables a consistent estimate of seasonal ozone loss from ground-based observations. The results highlight the ability of ground-based microwave radiometers to quantify chemical ozone depletion and its temporal evolution.

This study also demonstrates the value of ground-based measurements as an independent and complementary component of the global observing system, providing continuity and reducing reliance on satellite data for monitoring stratospheric ozone.

## 1 Introduction

Ozone is one of the most important trace gases in Earth's atmosphere, where it shields Earth's surface from the majority of the Sun's emitted ultraviolet radiation (UV). This shield, also called the Ozone layer, is formed through a series of photochemical reactions first proposed in Sidney Chapman's pioneering work *A Theory of Upper Atmospheric Ozone* (Chapman, 1930). In this cyclic event UV splits molecular oxygen into atomic oxygen, which reacts with molecular oxygen to form ozone. Further solar UV radiation breaks up the ozone molecule to form molecular and atomic oxygen again. Chapman predicted that this process would occur between 15-35 km, to form a layer of ozone, later on commonly described as the ozone layer. During the second half of the 20th century holes in the ozone layer began to form due to Ozone Depleting Substance (ODS) (Solomon et al., 1986; Farman and Gardiner, 1987). The absolute majority of the ODS gasses does not have a natural origin, but instead



was formed from human activities. This prompted the Montreal Protocol, banning industries and other actors to produce ODS (United Nations Environment Programme, 1987).

25 Since the signing of the Montreal Protocol, the global reduction of ozone-depleting substances has driven significant recovery of the ozone layer, with levels moving closer to their pre-industrial state (Solomon et al., 2016). At the same time, the deployment of satellite instruments such as the Microwave Limb Sounder (MLS) aboard NASA's Aura mission (Waters et al., 2006), along with ground-based microwave radiometers, has enhanced our ability to track ozone trends and confirm this recovery. One of these ground-based microwave radiometers is MIRA2 measuring ozone at 273 GHz, situated within the Arctic  
30 circle, at the Swedish Institute of Space Physics in Kiruna, Sweden.

Although stratospheric ozone shows an overall increasing trend, episodes of chemical ozone depletion still occur in the polar regions under winter atmospheric conditions. A key precursor is the extremely low temperature that develops within the polar vortex during the Arctic and Antarctic winters. One of the coldest and most stable Arctic polar vortices on record occurred during the winter of 2019–2020 (Manney et al., 2022).

35 In this study, we present the first ozone dataset from MIRA2 collected during the winter of 2019/2020. We first assess the consistency of MIRA2 against coincident Aura MLS observations through a comprehensive cross-comparison (Sect. 5.1). Then we use the consistent MIRA2 retrievals to independently quantify local cumulative chemical ozone depletion during this extraordinary winter (Sect. 5.2), placing our results in the context of previous studies (Manney et al., 2020; Wohltmann et al., 2021). These measurements illustrate the value of direct observational data for monitoring stratospheric ozone variability and  
40 chemical loss. As Aura MLS approaches the end of its operational lifetime, our work further highlights the need to maintain and expand independent observational capabilities, including ground-based microwave radiometry, to ensure long-term continuity and reliability of ozone records.

## 2 Previous Studies of the Northern Hemisphere Winter 2019/2020

The northern hemisphere (NH) winter of 2019/2020 exhibited one of the coldest and strongest stratospheric polar vortices on  
45 record, surpassing previously extreme winters such as 2011 (Manney et al., 2020). Persistently low planetary wave activity during December–February allowed the vortex to remain largely undisturbed (Lawrence et al., 2020), resulting in a strong and long-lived polar vortex. These conditions enabled substantial chemical ozone depletion—the most severe Arctic ozone loss observed to date—as consistently documented by both satellite observations and model simulations (Manney et al., 2020; Groöß and Müller, 2021; Wohltmann et al., 2021). Strong ozone loss is often confined to the coldest air masses within the polar  
50 vortex, a low pressure system in the stratosphere that is commonly identified using potential vorticity (PV)-based diagnostics. The polar vortex size and strength can be well represented by equivalent latitude coordinates (Nash et al., 1996). The polar vortex describes a strong transport barrier at the vortex edge, which effectively limits mixing with extra-vortex air and allows the chemical evolution of isolated air masses to be tracked over time (Manney et al., 1994).

Within this isolated and persistently cold part of the vortex, conditions were favorable for widespread formation of polar  
55 stratospheric clouds (PSC). These clouds, a mixture of supercooled liquid droplets and solid particles, enable heterogeneous



chemistry that activates chlorine and enhances ozone destruction. In particular, reservoir species such as HCl and ClONO<sub>2</sub> are converted into photo-labile forms, which upon sunlight exposure in springtime in polar regions release reactive chlorine radicals (e.g., ClO) that drive catalytic ozone loss cycles (Solomon, 1999). At the same time, denitrification through sedimentation of HNO<sub>3</sub> reduces reactive nitrogen, limiting chlorine deactivation and thereby prolonging ozone depletion (Wohltmann et al., 2021; Manney et al., 2020).

The 2019/2020 Arctic winter polar vortex formed early, was exceptionally cold and persistent. As a consequence of these conditions, ozone depletion began unusually early, already in late November to early December, driven by low stratospheric temperature and elevated active chlorine (Wohltmann et al., 2021; Manney et al., 2020). The prolonged period of favorable chemical conditions for ozone depletion led to peak ozone loss in mid-March 2020, as indicated by simulations. By late March, ozone mixing ratios had declined to values comparable to those typically observed in the Antarctic, with total losses approaching 2.8 ppmv and near-complete depletion at the 460 K potential temperature level (Manney et al., 2020; Wohltmann et al., 2021).

### 3 Instruments and data

#### 3.1 MIRA2

MIRA2 is a remote sensing microwave radiometer operated as a guest instrument at the Swedish Institute of space physics in Kiruna (67.84N, 20.41E, 425 m asl). MIRA2 is a heterodyne radiometer with a cryogenically cooled Schottky-diode mixer and has a system noise temperature  $T_{\text{sys}}$  of about 1250 K (Single Side Band, cooled to about 70 K). Measurements are obtained pointing North at an elevation angle between 7° and 55° depending on the tropospheric conditions. MIRA2 covers the frequency range 268 to 281 GHz, deploying an acousto-optical spectrometer with 2048 channels and a Fast-Fourier-Transform spectrometer (FFTS) with 8224 channels and 1.0 GHz and 1.5 GHz bandwidth, respectively. With the FFTS bandwidth and 180 kHz frequency resolution a vertical profile between 18 and 60 km can be achieved, with a vertical resolution of about 10 km at best. In the above mentioned frequency range, observation of HNO<sub>3</sub>, N<sub>2</sub>O, ClO and O<sub>3</sub> is possible. However, due to instrumental limitations MIRA2 has been operated continuously in ozone observation mode only. Here we use measurements of the ozone emission line at 273.05 GHz, the strongest emission line in the available frequency range.

#### 3.2 Microwave Limb Sounder

The Microwave Limb Sounder (MLS) aboard the Aura satellite is a microwave radiometer that measures a wide range of atmospheric trace gases over altitudes of approximately 5–120 km. It succeeds the MLS instrument on the Upper Atmosphere Research Satellite (UARS). Owing to extensive validation and continuous improvements in retrieval algorithms, MLS observations are widely regarded as a reliable reference dataset.

The limb-sounding geometry yields a vertical resolution for ozone retrievals of about 2.5–7 km (full width at half maximum, FWHM) covering the altitude range of 5–120 km, and an effective horizontal resolution of approximately 300 km. MLS



provides near-global coverage every three days. These characteristics must be considered in the analysis (see Sect. 4.3 for spatial screening and Sect. 4.4 for the application of MIRA2 averaging kernels).

90 In this study, we deploy Level 2 (v5.0) O<sub>3</sub> (Schwartz et al., 2020) products from MLS for the comparison between MIRA2 and MLS (Sect. 5.1), as well as MLS Level 2 (v5.0) ClO and N<sub>2</sub>O (Santee, 2021; Lambert, 2021) products for the quantification of ozone loss and for the interpretation of the ozone depletion observed with MIRA2 (Sect. 5.2).

### 3.3 Observational data and reanalysis

Ozone measurements were collected with MIRA2 between 1 October 2019 and 30 April 2020 at the Swedish Institute of Space Physics in Kiruna, Sweden, targeting the ozone emission line centered at 273.05 GHz (Johansson et al., 2026).

95 For the analysis and estimation of ozone loss from MIRA2 observations, it is essential to ensure that MIRA2 measurements occur within the polar vortex, which also holds for coincident measurements by MLS. In contrast to satellite measurements, ground-based measurements, such as those obtained from MIRA2, are limited to a fixed geographical location. As the polar vortex evolves in both position and shape over the course of the winter, observations at a given site may both sample air inside the vortex, within the vortex edge region, or outside the vortex altogether. This variability introduces intermittent influence  
100 from mixing processes, particularly in the vortex edge region, where ozone-rich air from lower latitudes can be advected into the measurement region (Raffalski et al., 2005).

Consequently, time series from ground-based instruments reflect a combination of vortex and extra-vortex conditions. To ensure that measurements used for ozone loss determination represent air masses within the polar vortex, ECMWF reanalysis data are used to identify whether MIRA2 observations were obtained inside the vortex. Further details on the data selection are  
105 given in Sect. 4.3.

## 4 Analysis and methodology

### 4.1 Atmospheric Radiative Transfer Simulator

The Atmospheric Radiative Transfer Simulator (ARTS) is an open-source software package written primarily in C++ that enables detailed simulation of radiative transfer through planetary atmospheres. ARTS includes a comprehensive line-by-line  
110 radiative transfer model and provides tools for forward modelling as well as atmospheric retrieval applications.

In this work, ARTS version 2.6 (Buehler et al., 2025) and its Python interface, pyARTS, are used to simulate the microwave emission spectra observed by MIRA2 and to retrieve the vertical volume mixing ratio (VMR) profile of ozone from measurements conducted during the winter 2019–2020 campaign.

### 4.2 Inversion model

115 Ozone retrievals from MIRA2 measurements are performed using an inversion model based on the Optimal Estimation Method (OEM) (Rodgers, 2000), implemented within the pyARTS framework. This statistical approach provides an optimal estimate of



the atmospheric state by combining measured spectra with a priori information and their associated uncertainties. The forward model, implemented in ARTS, describes the relationship between the atmospheric state vector and the measured radiances. The atmospheric state deployed covers approximately 0.5–78 km in altitude, with a nominal vertical resolution of about 2  
120 km. Averaging kernel matrices and measurement response diagnostics are calculated to quantify the vertical sensitivity and to characterize the information content of the retrieved ozone profiles.

Within the OEM framework, the retrieved state vector  $\hat{\mathbf{x}}$  is obtained by combining the measurement vector  $\mathbf{y}$  with the a priori state  $\mathbf{x}_a$  and their associated covariance matrices:

$$\hat{\mathbf{x}} = \mathbf{x}_a + \mathbf{S}_a \mathbf{K}^T (\mathbf{K} \mathbf{S}_a \mathbf{K}^T + \mathbf{S}_\epsilon)^{-1} (\mathbf{y} - \mathbf{K} \mathbf{x}_a), \quad (1)$$

125 where  $\mathbf{K}$  is the Jacobian matrix describing the sensitivity of the measurements to changes in the atmospheric state,  $\mathbf{S}_a$  is the a priori covariance matrix, and  $\mathbf{S}_\epsilon$  represents the measurement noise covariance. Measurement noise is assumed to be Gaussian and is estimated from the observed spectra.

A priori profiles for the retrieved species are primarily derived from the COSPAR International Reference Atmosphere (CIRA-86). For ozone, a climatology based on Version 8 IMK–IAA MIPAS ozone profiles, representative of the winter season  
130 for the latitude range of Kiruna, is used to provide a realistic description of the expected ozone distribution (Kiefer et al., 2023). The MIPAS  $\text{O}_3$  profile was scaled by 75% as this lead to stable and consistent retrievals. The a priori covariance for ozone varies with atmospheric pressure to balance the relative weighting between measurements and prior constraints. In regions with low measurement sensitivity, the retrieval is dominated by the a priori, while in regions with higher sensitivity it is primarily driven by the observed spectra.

### 135 4.3 Data selection

Coincident measurements between MIRA2 and MLS were identified based on combined temporal and spatial criteria. MLS observations were considered coincident if they occurred within  $\pm 4$  h of a MIRA2 measurement and within a 400 km radius of Kiruna. The resulting set of coincident measurements is shown in Fig. 1 (black).

Both datasets were subsequently filtered using retrieval quality criteria. For the MIRA2 observations, only measurements  
140 with an integration time of at least 1 h were retained to ensure a sufficient signal-to-noise ratio. Furthermore, retrievals were required to meet two conditions: (i) the residual between the fitted and observed spectra does not exceed 1 K, and (ii) the measurement response (MR) is  $\geq 0.8$ .

The measurement response describes the fraction of information in the retrieval that is provided by the measurement rather than the a priori, and thus quantifies the sensitivity of the retrieved profile to the true atmospheric state. It is derived from  
145 the averaging kernel matrix,  $\mathbf{A}$ , which characterizes the sensitivity of the retrieval to perturbations in the true state (Rodgers, 2000). The retrieved state  $\hat{\mathbf{x}}$  is given by

$$\hat{\mathbf{x}} = \mathbf{x}_a + \mathbf{A}(\mathbf{x} - \mathbf{x}_a), \quad (2)$$

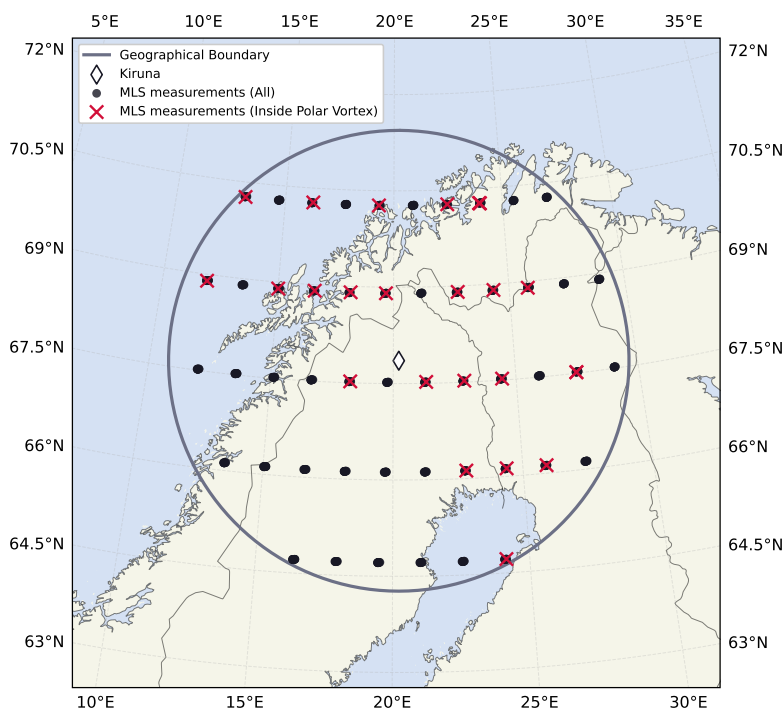


**Figure 1.** Black markers denote MLS observations that satisfy the temporal, spatial, and quality screening criteria (456 samples). Red crosses indicate coincident inside vortex observations (145 samples). The gray circle shows the flat projection of a circle centered on Kiruna with a radius of 400 km.

where  $\mathbf{x}$  denotes the true state and  $\mathbf{x}_a$  the a priori. The measurement response at pressure level  $i$  is defined as

$$MR_i = \sum_j A_{ij}. \quad (3)$$

150 Values of MR approaching unity indicate that the retrieved profiles are largely determined by the measurement rather than the a priori, whereas lower values indicate a stronger a priori influence. The applied threshold ( $MR \geq 0.8$ ), commonly used in atmospheric studies, ensures that at least 80% of the retrieved information originates from the measurement (Sauvageat et al., 2022).

155 For calculations of the chemically induced  $O_3$ , ECMWF reanalysis of potential vorticity was used to determine whether coincident MIRA2 and MLS measurements were conducted within the polar vortex. The criterion of Nash et al. (1996) was applied, and measurements satisfying this were classified as obtained inside the polar vortex (see Johansson et al. (2026)).



Moreover, for MLS data selection, recommended quality flags from the MLS Data Quality and Description (DQD) document (Livesey et al., 2022) were considered, which further constrained the dataset. To ensure that the measurements represent vortex-confined air, only observations identified as within the polar vortex in Johansson et al. (2026) were included for O<sub>3</sub> loss calculations (red crosses in Fig. 1).

#### 4.4 MLS smoothing and re-gridding

Due to the higher vertical resolution of the O<sub>3</sub> retrievals from MLS (see Sect. 3.2), a direct comparison with MIRA2 profiles is not meaningful. The MIRA2 retrievals exhibit a coarser vertical resolution, approximately 10–17 km, as illustrated in Fig. 2a. To ensure a consistent comparison, the MLS altitude resolution is therefore degraded using the averaging kernels from the MIRA2 retrievals. This procedure effectively smooths the MLS profiles to the vertical sensitivity and information content of MIRA2, enabling a physically meaningful comparison between the two datasets (von Clarmann and Glatthor, 2019). The smoothing procedure is expressed in Eq. 4, where  $\mathbf{x}_d$  denotes the degraded profile,  $\mathbf{x}_a$  and  $\mathbf{A}$  represent the a priori profile and averaging kernel from MIRA2, and  $\mathbf{x}_h$  is the high-resolution MLS profile.

$$\mathbf{x}_d = \mathbf{x}_a + \mathbf{A}(\mathbf{x}_h - \mathbf{x}_a) \quad (4)$$

For each comparison, the averaging kernel is selected by minimizing the temporal mismatch between coincident MLS and MIRA2 observations. Since the two datasets are defined on different pressure grids with different vertical sampling, the MLS profiles are first linearly interpolated in log-pressure space onto the MIRA2 retrieval grid, ensuring consistency between  $\mathbf{x}_a$ ,  $\mathbf{A}$ , and  $\mathbf{x}_h$  (von Clarmann and Glatthor, 2019). The effect of the interpolation and smoothing on the MLS profiles is illustrated in Fig. 2a, which shows the retrieved MIRA2 profile (black) alongside the original (blue) and smoothed (red) MLS profiles from a coincident measurement on 6 April 2020.

The vertical resolution, shown in Fig. 2b (black), is determined from the full width at half maximum (FWHM) of the averaging kernel rows (Rodgers, 2000), seen in Fig. 2c. The vertical representativeness of the retrieval is further characterized by the kernel offset (Fig. 2b, red), which quantifies the displacement between the nominal retrieval pressure level and the effective altitude from which measurement information predominantly originates. Small offsets indicate that the retrieved state is representative of the specified pressure level, whereas larger offsets imply substantial contributions from adjacent atmospheric layers. Where the measurement response (MR) exceeds 0.8 (Sauvageat et al., 2022), the offset is generally small, indicating that the retrieval is primarily constrained by the measurements and that the information is associated with approximately the correct pressure level. At lower MR values, the offset increases, reflecting a greater influence of the a priori constraints and a reduced vertical fidelity of the retrieval.

#### 4.5 Vertical coordinate for analysis

The cross-comparison and analysis of the retrieved profiles from MIRA2 are performed on the native retrieval grid (i.e. in pressure coordinates) in order to avoid interpolation artifacts and to ensure consistency with the original measurement sensitivity.

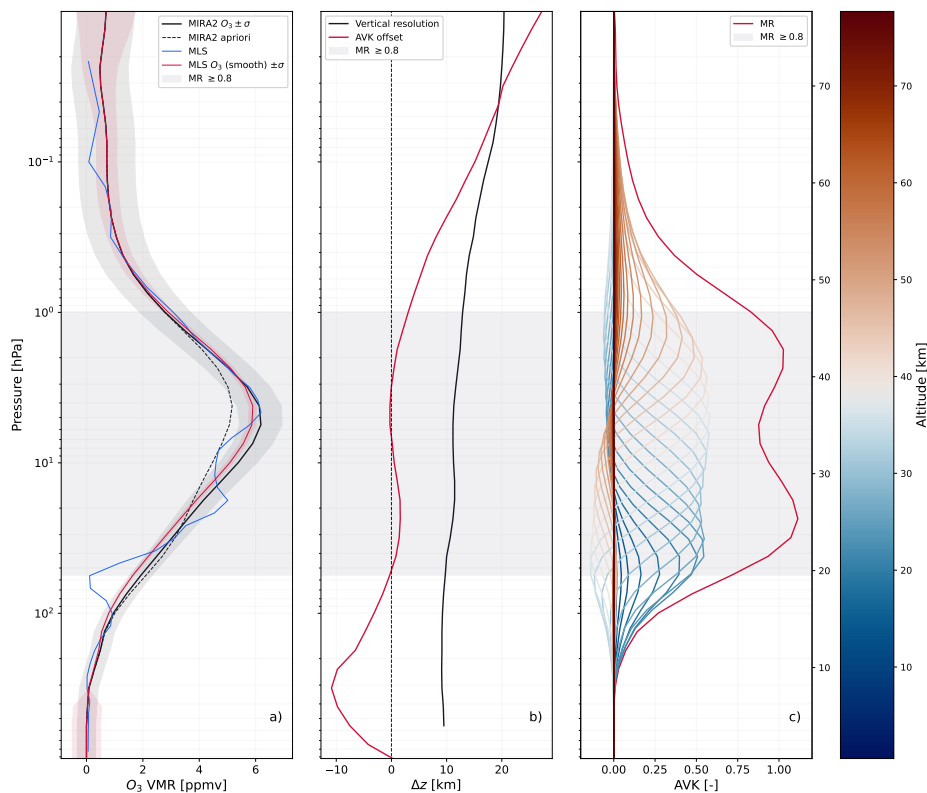


**Figure 2.** O<sub>3</sub> profiles from MIRA2 (Johansson et al., 2026) (black), original MLS (Schwartz et al., 2020) (blue), and smoothed MLS (red) with  $\pm\sigma$  uncertainty (shaded) are shown in panel (a). Panel (b) shows the vertical resolution (black) and averaging kernel offset (red). Panel (c) shows the averaging kernels with colors associated to nominal altitude and measurement response (red). All data are from coincident MIRA2 and MLS measurements of 6 April 2020 with shaded regions indicating altitudes with  $MR \geq 0.8$ .

Retaining the native grid is particularly advantageous for intercomparisons, as it preserves the vertical resolution and averaging kernel characteristics of the retrieval.

190 In contrast the ozone loss estimation is performed on isentropic surfaces of potential temperature,  $\theta$ , as has been done in previous studies of Arctic winter 2020 ozone depletion (Manney et al., 2020; Grooß and Müller, 2021). We adopt isentropic surfaces of  $\theta$  because they allow repeated measurements to be compared while minimizing the influence of diabatic processes (Baumgartner et al., 2020). By definition, the potential temperature accounts for the surrounding atmospheric temperature, as shown for dry air in Eq. 5, where  $T$  is the atmospheric temperature,  $p_0$  and  $p$  are the reference ground-level pressure and the local atmospheric pressure, respectively,  $R$  is the specific gas constant of dry air, and  $c_p$  is the specific heat capacity of dry air

$$\theta = T \left( \frac{p_0}{p} \right)^{R/c_p} \quad (5)$$



This implies that observed changes in an air parcel along an isentropic surface are primarily due to adiabatic motion. Consequently, temporal changes observed at a constant isentropic surface more reliably reflect dynamical and chemical processes. 200 This distinction is particularly important when estimating chemical ozone losses, as it allows us to separate changes in  $O_3$  caused by transport from those due to chemical reactions. Furthermore, the use of potential temperature as a vertical coordinate aligns our methodology with prior studies of the Arctic winter 2020, mentioned earlier in this section, facilitating direct comparison of results.

While  $\theta$  is directly available for all MLS data products through the DMP dataset (Millan et al., 2026), it is explicitly calcu- 205 lated for the MIRA2 measurements using Eq. 5. For this calculation, we employ the same temperature and pressure profiles from ECMWF that are used in the retrieval process, as described in Sect. 4.2. Subsequently, all MLS and MIRA2 data are interpolated onto a common potential temperature grid, enabling direct comparison between the datasets and facilitating ozone loss calculations on fixed isentropic surfaces.

#### 4.6 Ozone loss calculations

210 In this study, chemical ozone loss is quantified using the relationship between  $O_3$  and the long-lived tracer  $N_2O$ , commonly referred to as the tracer–tracer correlation method (Tilmes et al., 2006). This approach exploits the quasi-inert behavior of  $N_2O$  in the stratosphere on seasonal timescales, allowing it to serve as a robust proxy for transport-driven variability in  $O_3$ . By establishing a reference relationship between  $O_3$  and  $N_2O$  under conditions largely unaffected by chemical ozone depletion, deviations from this reference can be attributed to chemically induced ozone loss as long as air masses are not disturbed by 215 mixing processes.

The identification of an appropriate time period requires atmospheric conditions under which the polar vortex is dynamically well established, while chemically induced ozone depletion remains limited. Previous studies (Manney et al., 2020; Wohltmann et al., 2021) report enhanced ClO activation in late November and early December 2019, indicating the onset of halogen-driven  $O_3$  depletion. By mid-December, ClO concentrations decreased again, suggesting a temporary reduction in chemical ozone 220 loss. We therefore select 9 December 2019 as a representative period with minimal chemical depletion. Using coincident MLS  $N_2O$  and MIRA2  $O_3$  observations, we derive the  $N_2O$ – $O_3$  reference relationship from air masses within the polar vortex edge in the 400–600 K potential temperature range. This relationship is used to estimate passive ozone ( $O_{3P}$ ) during late winter and early spring from coincident MLS  $N_2O$  observations. The cumulative chemical ozone loss (Eq. 6) is defined as the difference between measured ozone from MIRA2 ( $O_{3M}$ ) and passive ozone.

$$225 \quad \Delta O_3 = O_{3M} - O_{3P} \quad (6)$$

## 5 Results and discussion

Before presenting the cumulative  $O_3$  loss derived from the winter 2019/2020 MIRA2 measurements (Sect. 5.2), we first assess the consistency of the MIRA2 retrievals through comparison with coincident MLS observations.

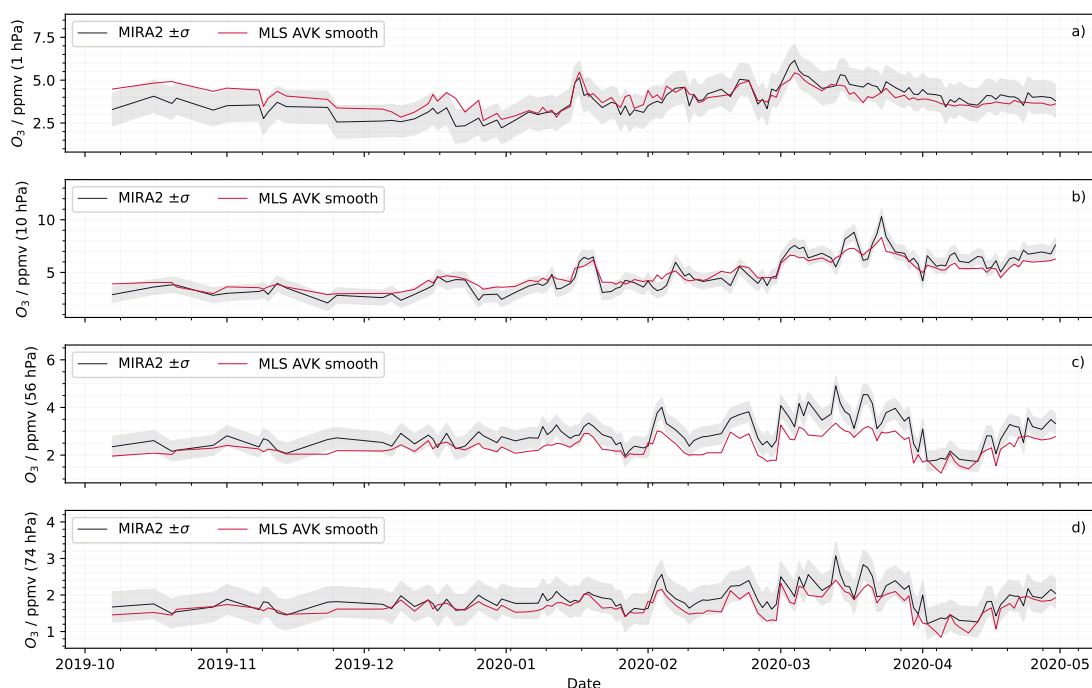


**Figure 3.** Comparison of coincident  $O_3$  measurements from MIRA2 (Johansson et al., 2026) and MLS (Schwartz et al., 2020) between 1 October 2019 and 30 April 2020 at four pressure levels: 1, 10, 56, and 74 hPa (panels a–d). The solid black line shows MIRA2 measurements, with shaded areas indicating  $\pm\sigma$ , reflecting total retrieval uncertainty. The solid red line shows MLS measurements smoothed with the MIRA2 averaging kernel (see Sect. 4.4).

### 5.1 MIRA2 and MLS comparisons

230 Comparisons over the full measurement period focus on four representative pressure levels (1, 10, 56, and 74 hPa; Fig. 3), selected where MIRA2 exhibits sufficient measurement response (MR). No distinction is made between air masses inside or outside the polar vortex; all coincident measurements are included to assess the robustness of the spatiotemporal coincidence criteria and the consistency of retrievals in mixed air masses.

235 Figure 3 shows generally good agreement across all levels, with MLS typically falling within the  $\pm\sigma$  range of MIRA2. At 56 hPa (Fig. 3c), MIRA2 slightly overestimates  $O_3$ , whereas at 1 and 10 hPa (Figs. 3a–b), a temporal shift is visible: early in the period, MIRA2 underestimates  $O_3$ , while later it overestimates. The agreement is best at 74 hPa (Fig. 3d). Overall, retrievals contain sufficient information content throughout the period.

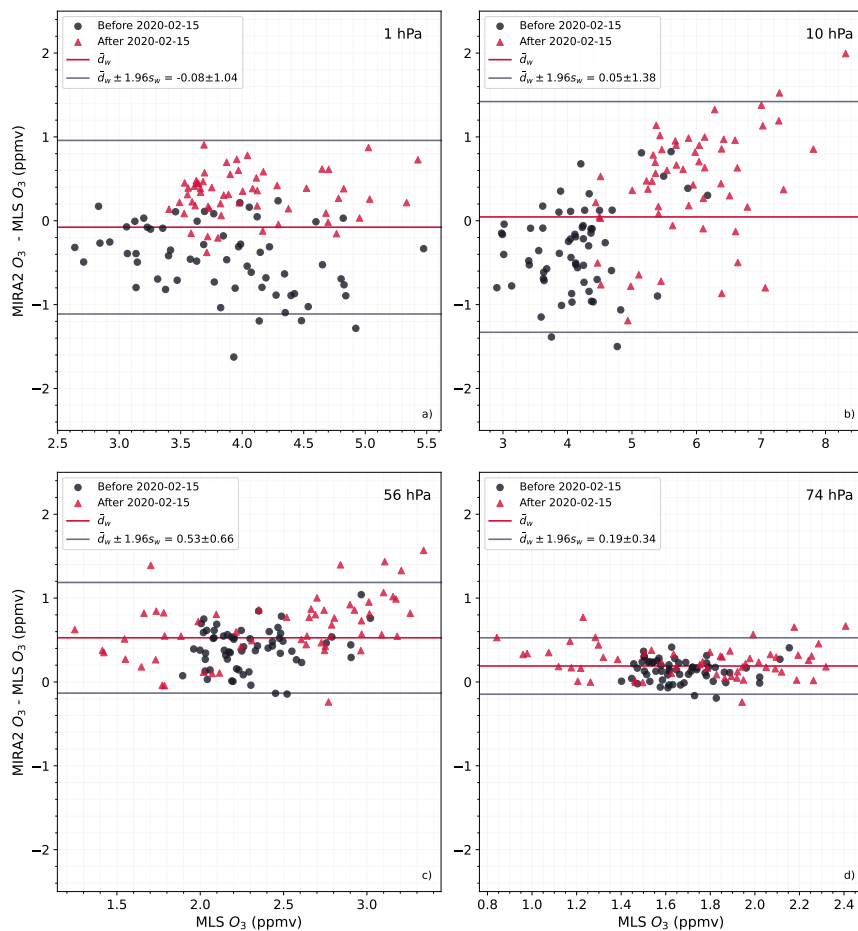


**Figure 4.** Modified Bland–Altman plots showing weighted differences in  $O_3$  (MIRA2 - MLS) at 1, 10, 56, and 74 hPa (panels a–d). Black points indicate observations before 15 February 2020 and red triangles after. The red line denotes the weighted mean bias  $\bar{d}_w$ , and the gray lines indicate the limits of agreement,  $\bar{d}_w \pm 1.96s_w$ , representing the range in which 95% of individual differences are expected to lie under an approximately Gaussian distribution (Bland and Altman, 1986).

To further quantify the agreement between the two data sets, we applied a modified Bland–Altman analysis (Appendix A1) that accounts for the varying uncertainty of individual measurements. Figure 4 shows the weighted differences (MIRA2 - MLS) as a function of MLS  $O_3$ , with the *weighted mean bias* ( $\bar{d}_w$ ) and the *limits of agreement* ( $\bar{d}_w \pm 1.96s_w$ ) indicated.

The Bland–Altman analysis supports the general agreement in Fig. 3. At 1 and 10 hPa, mean differences are small (Table 1), and the majority of points lies within the 95% limits of agreement ( $\pm 1.96s_w$ ). This provides a quantitative measure of overall agreement across the dataset. Temporal shifts are evident: MIRA2 underestimates  $O_3$  before 15 February 2020 and overestimates it afterward. At 10 hPa, a weak magnitude-dependent bias appears, with higher MLS values being slightly overestimated by MIRA2. This could stem from a priori influence at 1 and 10 hPa, as a consequence of our approach of using a fixed  $O_3$



**Table 1.** Summary of the statistics for the comparison between MIRA2 and MLS.  $\bar{d}_w$  denotes the weighted mean difference (MIRA2 - MLS),  $s_w$  the standard deviation of the weighted differences, and  $r$  the Pearson correlation coefficient.

Pressure level [hPa]	$\bar{d}_w$ [ppmv]	$s_w$ [ppmv]	$r$
1	-0.08	0.53	0.74
10	0.05	0.70	0.95
56	0.53	0.34	0.89
74	0.19	0.17	0.87

a priori not adjusted over the measurement period. At 56 and 74 hPa, larger differences occur, likely due to interpolating MLS onto MIRA2's pressure grid and smoothing with the averaging kernel. Nevertheless, the majority of observations remains within the weighted limits of agreement, demonstrating overall consistency with MLS across the measurement period.

Correlation analysis (Appendix A2) further supports the comparison, with linear correlation coefficients exceeding  $r > 0.7$  at all pressure levels (Table 1). Taken together, these results demonstrate that MIRA2 retrievals are internally consistent and in good agreement with MLS, providing a robust basis for subsequent ozone loss calculations.

## 5.2 Ozone loss calculations at 475 K

For the calculation of observed ozone loss, we adopt potential temperature as the vertical coordinate, as described in Sect. 4.5. This choice facilitates direct comparison with previous studies of ozone depletion during winter 2019/2020 (Manney et al., 2020; Grooß and Müller, 2021).

We focus our analysis on the 475 K isentropic surface, selected based on two considerations. First, previous studies report maximum ozone loss near 460 K (Manney et al., 2020). Second, MIRA2 retrievals exhibit increasing a priori influence below approximately 475 K, reducing measurement sensitivity. The 475 K level therefore represents a compromise between capturing near-maximum depletion and ensuring sufficient measurement sensitivity for a robust retrieval.

Figure 5a shows coincident daily mean ClO volume mixing ratios from MLS (Santee, 2021), while Fig. 5b presents the corresponding  $O_3$  time series at 475 K from MIRA2. Measurements within the polar vortex are indicated by red crosses, and white markers denote dates when MIRA2 sampled vortex air masses. Due to the limited number of observations within the polar vortex, loss rates cannot be robustly derived, and the period of peak modeled loss (mid-March; Wohltmann et al. 2021) is not fully captured. This limited sampling reflects a fundamental constraint of ground-based measurement at a fixed location: loosening the vortex edge criteria could introduce extra-vortex air masses into the analysis, where mixing with ozone-rich mid-latitude air would bias the derived loss toward smaller values. The selected threshold therefore represents a deliberate trade-off between sampling frequency and the representativeness of the retrieved chemical ozone loss. Nevertheless, the dataset allows estimation of cumulative ozone loss over the winter and identification of the seasonal  $O_3$  minimum. While the temporal sampling does not fully resolve the period of peak chemical loss, the tracer-based framework still allows following the cumulative ozone depletion, making the derived loss estimate less sensitive to data gaps in direct observations.



275 periods of strong mixing.

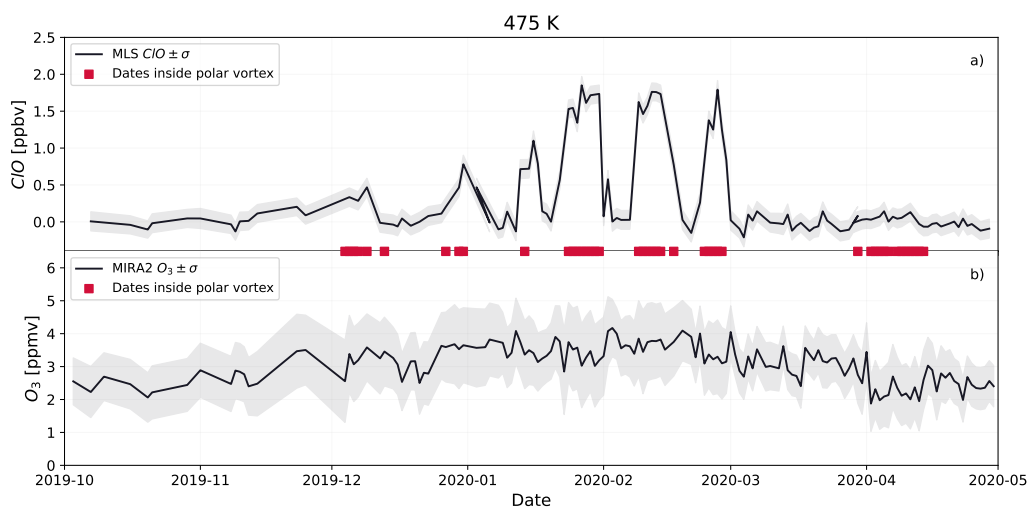


**Figure 5.** Time series of coincident mid-day ( $12 : 00 \pm 4h$  UTC) MLS ClO (Santee, 2021) (a) and MIRA2 (Johansson et al., 2026) O<sub>3</sub> (b) volume mixing ratio observed at the 475 K isentropic level. The black line shows daily means, and the shaded region denotes  $\pm 1\sigma$  variability over the full measurement period. Dates on which measurements were obtained within the polar vortex are indicated by red squares.

The periods when Kiruna is located within the polar vortex edge or core are associated with reduced O<sub>3</sub> values in MIRA2 measurements (Fig. 5b), most notably in late February and early April 2020. During February and March, these periods also show enhanced ClO volume mixing ratios, consistent with chlorine activation in isolated vortex air masses and in agreement with previous studies (Manney et al., 2020; Wohltmann et al., 2021). Obviously, the observed O<sub>3</sub> variability is linked to chemical processing within vortex-confined air masses.

A notable feature is that minimum O<sub>3</sub> occurs in early April (Fig. 5b), when ClO levels are already low (Fig. 5a). This indicates a temporal decoupling between active chlorine chemistry and accumulated ozone loss as already pointed out by Wohltmann et al. (2021). The air masses sampled by MIRA2 have undergone substantial depletion during the period of peak ClO activation in mid-March 2020, driven by temperatures below the threshold for PSC formation combined with increasing solar radiation enabling efficient catalytic O<sub>3</sub> destruction (Wohltmann et al., 2021). By early April, ClO has largely been deactivated, while significant ozone production has not yet resumed. Consequently, the observations represent air that has experienced prior chemical depletion rather than ongoing ozone loss.

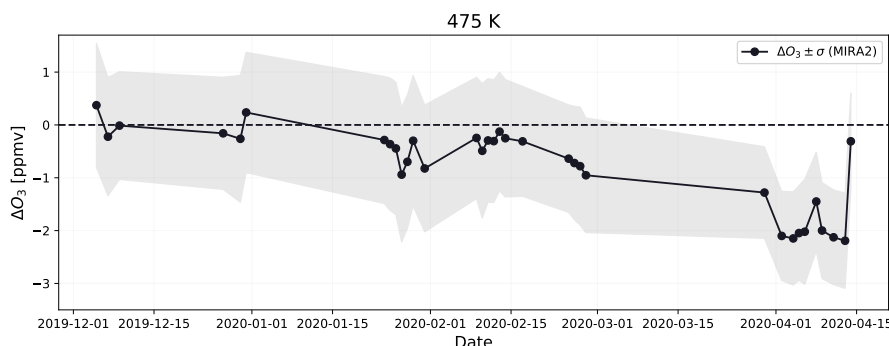


**Figure 6.** Cumulative ozone loss ( $\Delta O_3$ ) at the 475 K isentropic level derived from MIRA2 observations (Johansson et al., 2026). The loss is calculated using Eq. 6 for measurements classified as being within the polar vortex.

Figure 6 shows a steady ozone loss from late winter into early spring, with a more pronounced decline during March and early April, consistent with enhanced halogen-driven chemistry under persistent cold vortex conditions. The cumulative chemically induced ozone loss reaches  $2.19 \pm 0.90$  ppmv at 475 K from December 2019 until the first half of April 2020. The shaded area in 6 reflects the propagated retrieval uncertainty in MIRA2 ozone, including measurement noise and smoothing effects.

Previous studies report maximum chemical  $O_3$  losses of up to 2.8 ppmv below 460 K (Manney et al., 2020), with near-complete depletion and minimum values of 0.2 ppmv at 450 K (Wohltmann et al., 2021). Scaling reported MLS peak losses to the 475 K level, we find that the peak losses derived from MIRA2 are in good agreement and remain within the estimated retrieval uncertainty.

This agreement provides confidence to both the MIRA2 measurements and the applied retrieval methodology. It further indicates that ground-based microwave observations are capable of capturing the magnitude and seasonal evolution of extreme Arctic ozone depletion. These results complement satellite-based estimates by providing an independent and sound ground-based perspective, despite the limited temporal sampling within the polar vortex.

## 6 Conclusions

In this study, ground-based microwave observations from MIRA2 were used to investigate Arctic stratospheric ozone during the winter 2019/2020 and to compare with coincident ozone observations from Aura MLS. We also quantified chemical ozone loss on isentropic surfaces from MIRA2 observations.

Comparison with coincident MLS measurements shows that MIRA2 retrievals are consistent across the investigated pressure levels, with rather small biases and without statistically significant differences. This agreement demonstrates that MIRA2 provides reliable ozone measurements with sufficient information content for quantitative analysis of stratospheric variability.



Using a tracer-based framework, cumulative chemically induced ozone loss was derived at the 475 K isentropic level. The results show a steady increase in ozone loss from late winter into early spring, reaching  $2.19 \pm 0.9$  ppmv in early April 2020. The timing and magnitude of the loss are consistent with the exceptional Arctic ozone depletion reported by other studies.

The observed temporal offset between peak ClO and minimum O<sub>3</sub> highlights the cumulative nature of chemical ozone loss and reflects the evolution of chlorine activation and deactivation within the polar vortex. This behavior is consistent with the established understanding of halogen-driven ozone depletion under cold and sunlit conditions in air-masses confined within a long lasting polar vortex.

Despite limited temporal sampling of vortex air masses, the tracer-based approach enables reconstruction of seasonal ozone loss, reducing sensitivity to observational gaps. This demonstrates the capability of ground-based microwave radiometers to capture both the magnitude and temporal evolution of Arctic ozone depletion events.

Overall, this study shows that MIRA2 provides consistent and reliable stratospheric ozone retrievals, in good agreement with MLS and previous analyses of the 2019/2020 Arctic winter. Combining data from MIRA2 with MLS allows the construction of tracer–tracer relationships and the temporal and spatial identification of polar vortex air masses, demonstrating the value of direct observational data for quantifying chemical ozone loss. These results highlight the critical role of comprehensive measurements in capturing stratospheric variability, while also revealing the current reliance on a limited set of observing systems. As MLS approaches the end of its operational lifetime, maintaining and expanding observational capabilities is essential. Increasing the range of tracers relevant for stratospheric chemistry would reduce dependence on model assumptions and strengthen observational constraints on ozone variability and recovery.



## Appendix A: Statistics

### A1 Weighted Bland–Altman analysis

We compare coincident daily mean measurements from MIRA2 ( $G_i$ ) and MLS ( $S_i$ ) using a weighted Bland–Altman approach, where individual differences are weighted by their combined uncertainty. Pointwise uncertainties from MIRA2 and MLS are  
330 assumed independent:

$$\sigma_{C_i} = \sqrt{\sigma_{G_i}^2 + \sigma_{S_i}^2}. \quad (\text{A1})$$

For each coincident pair:

$$M_i = \frac{G_i + S_i}{2}, \quad (\text{A2})$$

$$D_i = G_i - S_i. \quad (\text{A3})$$

335 The weight for each observation is the inverse of the squared combined uncertainty:

$$w_i = \frac{1}{\sigma_{C_i}^2}. \quad (\text{A4})$$

The weighted mean difference (bias) is:

$$\bar{d}_w = \frac{\sum_i w_i D_i}{\sum_i w_i}, \quad (\text{A5})$$

and the weighted variance of differences is

$$340 \quad s_w^2 = \frac{\sum_i w_i (D_i - \bar{d}_w)^2}{\sum_i w_i - \frac{\sum_i w_i^2}{\sum_i w_i}}. \quad (\text{A6})$$

Assuming approximate Gaussianity, the 95% limits of agreement are defined as

$$\text{LoA} = \bar{d}_w \pm 1.96 s_w. \quad (\text{A7})$$

These limits provide a practical range in which 95% of individual differences are expected to lie, incorporating both systematic bias and random variability while accounting for measurement uncertainties that vary across observations (Bland and  
345 Altman, 1986; Myles and Cui, 2007).

### A2 Correlation analysis

To complement the Bland–Altman analysis, we evaluated the linear relationship between coincident  $O_3$  measurements from MIRA2 and MLS using the Pearson correlation coefficient,  $r$ . For paired observations  $\{G_i, S_i\}$ , the Pearson  $r$  is defined as

$$r = \frac{\sum_i (G_i - \bar{G})(S_i - \bar{S})}{\sqrt{\sum_i (G_i - \bar{G})^2} \sqrt{\sum_i (S_i - \bar{S})^2}}, \quad (\text{A8})$$



350 where  $\bar{G}$  and  $\bar{S}$  are the sample means of the MIRA2 and MLS measurements, respectively.

Pearson  $r$  quantifies the strength and direction of the linear association between the two datasets, with  $r = 1$  indicating perfect positive linear correlation,  $r = 0$  indicating no linear correlation, and  $r = -1$  indicating perfect negative linear correlation. The statistical significance of  $r$  can be assessed under the null hypothesis of no correlation.

355 Pearson correlation coefficients are widely used in atmospheric remote sensing intercomparisons to assess the consistency of co-located measurements (Steinbrecht et al., 2009; Tummon et al., 2015). While high  $s$  does not imply perfect agreement in magnitude (see related bias and limits of agreement in Appendix A1), it adds confidence that the temporal and vertical variability observed by MIRA2 is consistent with MLS observations.

*Data availability.* Aura MLS datasets can be found at <https://acdisc.gesdisc.eosdis.nasa.gov/data/>. Measurement, and retrieval data from MIRA2 is accessible from: <https://zenodo.org/records/19608988>. The MIRA2 dataset also contain flags whether measurements have been  
360 conducted within the polar vortex.

*Author contributions.* RJ contributed with analysis, data curation, visualization, software and writing the original draft. MM and UR both contributed with analysis and interpretation of the data. JG and UR provided MIRA2 measurement data

*Competing interests.* The authors declare that they have no conflict of interest



## References

- 365 Baumgartner, M., Weigel, R., Harvey, A. H., Plöger, F., Achatz, U., and Spichtinger, P.: Reappraising the appropriate calculation of a common meteorological quantity: potential temperature, *Atmospheric Chemistry and Physics*, 20, 15 585–15 616, <https://doi.org/10.5194/acp-20-15585-2020>, 2020.
- Bland, J. M. and Altman, D. G.: Statistical methods for assessing agreement between two methods of clinical measurement, *The Lancet*, 1, 307–310, [https://doi.org/10.1016/S0140-6736\(86\)90837-8](https://doi.org/10.1016/S0140-6736(86)90837-8), 1986.
- 370 Buehler, S. A., Larsson, R., Lemke, O., Pfreundschuh, S., Brath, M., Adams, I., Fox, S., Roemer, F. E., Czarnecki, P., and Eriksson, P.: The atmospheric radiative transfer simulator ARTS, version 2.6 — Deep python integration, *Journal of Quantitative Spectroscopy and Radiative Transfer*, 341, 109 443, <https://doi.org/https://doi.org/10.1016/j.jqsrt.2025.109443>, 2025.
- Chapman, S.: A Theory of Upper Atmospheric Ozone, *Memoirs of the Royal Meteorological Society*, 3, 103–125, 1930.
- Farman, J. C. and Gardiner, B. G.: Ozone depletion over Antarctica, *Nature*, 329, 574–574, <https://doi.org/10.1038/329574b0>, 1987.
- 375 Groöß, J.-U. and Müller, R.: Simulation of Record Arctic Stratospheric Ozone Depletion in 2020, *Journal of Geophysical Research: Atmospheres*, 126, e2020JD033 339, <https://doi.org/https://doi.org/10.1029/2020JD033339>, e2020JD033339 2020JD033339, 2021.
- Johansson, R., Raffalski, U., and Jochen, G.: MIRA2 measurement and retrieval data from 20191001-20200501, <https://doi.org/10.5281/zenodo.19608988>, 2026.
- Kiefer, M., von Clarmann, T., Funke, B., García-Comas, M., Glatthor, N., Grabowski, U., Höpfner, M., Kellmann, S., Laeng, A., Linden, A.,
- 380 López-Puertas, M., and Stiller, G. P.: Version 8 IMK-IAA MIPAS ozone profiles: nominal observation mode, *Atmospheric Measurement Technique*, 16, 1443–1460, <https://doi.org/10.5194/amt-16-1443-2023>, 2023.
- Lambert, A.: MLS/Aura Level 2 Nitrous Oxide (N<sub>2</sub>O) Mixing Ratio V005, <https://doi.org/10.5067/AURA/MLS/DATA2515>, 2021.
- Lawrence, Z. D., Perlwitz, J., Butler, A. H., Manney, G. L., Newman, P. A., Lee, S. H., and Nash, E. R.: The Remarkably Strong Arctic Stratospheric Polar Vortex of Winter 2020: Links to Record-Breaking Arctic Oscillation and Ozone Loss, *Journal of Geophysical Research: Atmospheres*, 125, e2020JD033 271, <https://doi.org/https://doi.org/10.1029/2020JD033271>, e2020JD033271 10.1029/2020JD033271, 2020.
- 385 Livesey, N. J., Read, W. G., Wagner, P. A., Froidevaux, L., Santee, M. L., Schwartz, M. J., Lambert, A., Millán Valle, L. F., Pumphrey, H. C., Manney, G. L., Fuller, R. A., Jarnot, R. F., Knosp, B. W., and Lay, R. R.: Earth Observing System (EOS) Microwave Limb Sounder (MLS) Version 5.0x Level 2 and Level 3 Data Quality and Description Document, Technical report / data quality document, Jet Propulsion Laboratory, California Institute of Technology, [https://doi.org/10.5067/AURA/MLS/DOC/V5\\_DATAQUALITYDOCUMENT](https://doi.org/10.5067/AURA/MLS/DOC/V5_DATAQUALITYDOCUMENT), nASA Goddard
- 390 Earth Sciences Data and Information Services Center, 2022.
- Manney, G. L., Zurek, R. W., O'Neill, A., and Swinbank, R.: On the Motion of Air through the Stratospheric Polar Vortex, *Journal of Atmospheric Sciences*, 51, 2973 – 2994, [https://doi.org/10.1175/1520-0469\(1994\)051<2973:OTMOAT>2.0.CO;2](https://doi.org/10.1175/1520-0469(1994)051<2973:OTMOAT>2.0.CO;2), 1994.
- Manney, G. L., Livesey, N. J., Santee, M. L., Froidevaux, L., Lambert, A., Lawrence, Z. D., Millán, L. F., Neu, J. L.,
- 395 Read, W. G., Schwartz, M. J., and Fuller, R. A.: Record-Low Arctic Stratospheric Ozone in 2020: MLS Observations of Chemical Processes and Comparisons With Previous Extreme Winters, *Geophysical Research Letters*, 47, e2020GL089 063, <https://doi.org/https://doi.org/10.1029/2020GL089063>, e2020GL089063 10.1029/2020GL089063, 2020.
- Manney, G. L., Millán, L. F., Santee, M. L., Wargan, K., Lambert, A., Neu, J. L., Werner, F., Lawrence, Z. D., Schwartz, M. J., Livesey, N. J., and Read, W. G.: Signatures of Anomalous Transport in the 2019/2020 Arctic Stratospheric Polar Vortex, *Journal of Geophysical Research: Atmospheres*, 127, e2022JD037 407, <https://doi.org/https://doi.org/10.1029/2022JD037407>, e2022JD037407 2022JD037407,
- 400 2022.



- Millan, V., Luis, F., and Manney, G. L.: MLS/Aura Level 2 Derived Meteorological Products for GEOS-IT 5.29.4 V005, <https://doi.org/10.5067/AURA/MLS/DATA2525>, 2026.
- Myles, P. S. and Cui, J.: Using the Bland–Altman method to measure agreement with repeated measures, *British Journal of Anaesthesia*, 99, 309–311, <https://doi.org/10.1093/bja/aem274>, 2007.
- 405 Nash, E. R., Newman, P. A., Rosenfield, J. E., and Schoeberl, M. R.: An objective determination of the polar vortex using Ertel’s potential vorticity, *J. Geophys. Res.*, 101, 9471–9478, <https://doi.org/10.1029/96JD00066>, 1996.
- Raffalski, U., Hochschild, G., Kopp, G., and Urban, J.: Evolution of stratospheric ozone during winter 2002/2003 as observed by a ground-based millimetre wave radiometer at Kiruna, Sweden, *Atmospheric Chemistry and Physics*, 5, 1399–1407, <https://doi.org/10.5194/acp-5-1399-2005>, 2005.
- 410 Rodgers, C. D., ed.: *Inverse Methods for Atmospheric Sounding: Theory and Practice*, World Scientific Publishing, ISBN-10 981022740X, 2000.
- Santee, M.: MLS/Aura Level 2 Chlorine Monoxide (ClO) Mixing Ratio V005, <https://doi.org/10.5067/AURA/MLS/DATA2505>, 2021.
- Sauvageat, E., Maillard Barras, E., Hocke, K., Haefele, A., and Murk, A.: Harmonized retrieval of middle atmospheric ozone from two microwave radiometers in Switzerland, *Atmospheric Measurement Techniques*, 15, 6395–6417, <https://doi.org/10.5194/amt-15-6395-2022>,  
415 2022.
- Schwartz, M. J., Froidevaux, L., Livesey, N. J., and Read, W. G.: MLS/Aura Level 2 Ozone (O<sub>3</sub>) Mixing Ratio V005, <https://doi.org/10.5067/Aura/MLS/DATA2516>, 2020.
- Solomon, S.: Stratospheric ozone depletion: A review of concepts and history, *Reviews of Geophysics*, 37, 275–316, <https://doi.org/https://doi.org/10.1029/1999RG900008>, 1999.
- 420 Solomon, S., Garcia, R. R., Rowland, F. S., and Wuebbles, D. J.: On the depletion of Antarctic ozone, *Nature*, 321, 755–758, <https://doi.org/10.1038/321755a0>, 1986.
- Solomon, S., Ivy, D. J., Kinnison, D., Mills, M. J., Neely, R. R., and Schmidt, A.: Emergence of healing in the Antarctic ozone layer, *Science*, 353, 269–274, <https://doi.org/10.1126/science.aae0061>, 2016.
- Steinbrecht, W., McGee, T., Twigg, L., Claude, H., Schöenborn, F., Sumnicht, G., and Silbert, D.: Intercomparison of stratospheric ozone  
425 and temperature profiles during the October 2005 Hohenpeißenberg Ozone Profiling Experiment (HOPE), *Atmospheric Measurement Techniques*, 2, 125–145, <https://doi.org/10.5194/amt-2-125-2009>, 2009.
- Tilmes, S., Müller, R., Groß, J.-U., Nakajima, H., and Sasano, Y.: Development of tracer relations and chemical ozone loss during the setup phase of the polar vortex, *Journal of Geophysical Research: Atmospheres*, 111, <https://doi.org/https://doi.org/10.1029/2005JD006726>, 2006.
- 430 Tummon, F., Hassler, B., Harris, N., Staehelin, J., Steinbrecht, W., Anderson, J., et al.: Intercomparison of vertically resolved merged satellite ozone data sets: interannual variability and long-term trends, *Atmospheric Chemistry and Physics*, 15, 3021–3043, <https://doi.org/10.5194/acp-15-3021-2015>, 2015.
- United Nations Environment Programme: *Montreal Protocol on Substances that Deplete the Ozone Layer*, <https://ozone.unep.org/treaties/montreal-protocol>, adopted in Montreal on 16 September 1987, entered into force on 1 January 1989, 1987.
- 435 von Clarmann, T. and Glatthor, N.: The application of mean averaging kernels to mean trace gas distributions, *Atmospheric Measurement Techniques*, 12, 5155–5160, <https://doi.org/10.5194/amt-12-5155-2019>, 2019.
- Waters, J., Froidevaux, L., Harwood, R., Jarnot, R., Pickett, H., Read, W., Siegel, P., Cofield, R., Filipiak, M., Flower, D., Holden, J., Lau, G., Livesey, N., Manney, G., Pumphrey, H., Santee, M., Wu, D., Cuddy, D., Lay, R., Loo, M., Perun, V., Schwartz, M., Stek, P., Thurstans,



- 440 R., Boyles, M., Chandra, K., Chavez, M., Chen, G.-S., Chudasama, B., Dodge, R., Fuller, R., Girard, M., Jiang, J., Jiang, Y., Knosp, B.,  
LaBelle, R., Lam, J., Lee, K., Miller, D., Oswald, J., Patel, N., Pukala, D., Quintero, O., Scaff, D., Van Snyder, W., Tope, M., Wagner, P.,  
and Walch, M.: The Earth observing system microwave limb sounder (EOS MLS) on the aura Satellite, *IEEE Transactions on Geoscience  
and Remote Sensing*, 44, 1075–1092, <https://doi.org/10.1109/TGRS.2006.873771>, 2006.
- 445 Wohltmann, I., von der Gathen, P., Lehmann, R., Deckelmann, H., Manney, G. L., Davies, J., Tarasick, D., Jepsen, N., Kivi, R., Lyall, N.,  
and Rex, M.: Chemical Evolution of the Exceptional Arctic Stratospheric Winter 2019/2020 Compared to Previous Arctic and Antarctic  
Winters, *Journal of Geophysical Research: Atmospheres*, 126, e2020JD034356, <https://doi.org/https://doi.org/10.1029/2020JD034356>,  
e2020JD034356 2020JD034356, 2021.